Biochimica et Biophysica Acta 1777 (2008) 834–846

Contents lists available at ScienceDirect

Biochimica et Biophysica Acta

journal homepage: www.elsevier.com/locate/bbabio

Mitochondrial oxidative phosphorylation and energetic status are reflected by morphology of mitochondrial network in INS-1E and HEP-G2 cells viewed by 4Pi microscopy

Lydie Plecitá-Hlavatá [a], Mark Lessard [b], Jitka Šantorová [a], Joerg Bewersdorf [b], Petr Ježek [a,*]

[a] Department of Membrane Transport Biophysics, No. 75, Institute of Physiology, Academy of Sciences of the Czech Republic, Vídeňská 1083, 14220 Prague 4, Czech Republic
[b] Institute for Molecular Biophysics, The Jackson Laboratory, Bar Harbor, Maine, USA

ARTICLE INFO

Article history:
Received 30 January 2008
Received in revised form 31 March 2008
Accepted 1 April 2008
Available online 10 April 2008

Keywords:
3D morphology of mitochondrial network
4Pi microscopy
Uncoupling
Oxidative phosphorylation
Insulinoma INS-1E cell
Hepatocellular carcinoma HEP-G2 cell

ABSTRACT

Mitochondria in numerous cell types, especially in cultured cells, form a reticular network undergoing constant fusion and fission. The three dimensional (3D) morphology of these networks however has not been studied in detail to our knowledge. We have investigated insulinoma INS-1E and hepatocellular carcinoma HEP-G2 cells transfected with mitochondria-addressed GFP. Using 4Pi microscopy, 3D morphology changes responding to decreased oxidative phosphorylation and/or energetic status could be observed in these cells at an unprecedented 100 nm level of detail. In INS-1E cells cultivated at 11 mM glucose, the mitoreticulum appears predominantly as one interconnected mitochondrion with a nearly constant 262±26 nm tubule diameter. If cultured at 5 mM glucose, INS-1E cells show 311±36 nm tubules coexisting with numerous flat cisternae. Similar interconnected 284±38 nm and 417±110 nm tubules were found in HEP-G2 cells cultivated at 5 mM and hyperglycaemic 25 mM glucose, respectively. With rotenone inhibiting respiration to ~10%, disintegration into several reticula and numerous ~300 nm spheres or short tubules was observed. De-energization by uncoupling additionally led to formation of rings and bulky cisternae of 1.4±0.4 μm diameter. Rotenone and uncoupler acted synergically in INS-1E cells and increased fusion (ongoing with fission) forming bowl-like shapes. In HEP-G2 cells fission partially ceased with FCCP plus rotenone. Thus we have revealed previously undescribed details for shapes upon mitochondrial disintegration and clearly demonstrate that high resolution 3D microscopy is required for visualization of mitochondrial network. We recommend 4Pi microscopy as a new standard.

1. Introduction

Mitochondria are currently recognized not only as the cell's powerhouse, but also as important modulators in the molecular physiology of the cell. The impairment of their function most frequently leads to oxidative stress causing cellular dysbalance or initiation of various forms of cell death, both being dominating processes in pathophysiology of numerous diseases and aging [1–9]. The oxidative stress stems in many cases from the elevated mitochondrial superoxide production [8]. Moderate elevation of superoxide levels may participate in redox signaling, whereas repeated strongly self-accelerating oxidative stress might disrupt redox homeostasis in certain diseases and aging. Frequently, oxidative stress comes from electron transfer retardation, hence respiratory inhibition [8].

Predominantly, textbook images of mitochondrial morphology based on electron micrographs are represented by solitary shapes, which we now consider as sections of mitochondrial tubules. These kidney shaped organelles typically exhibit inner structures of folded sheet-like cristae [10]. Recent electron tomography data has however revealed different cristae shapes [11], showing that the inner membrane forms "sacks" with bottleneck outlets proximal to the outer membrane. Pioneering observations of Hackenbrock more than 40 years ago [10] revealed rapid and reversible changes of the mitochondria cristae shapes from the so-called "orthodox" to "condensed" conformations upon activation of ATP synthesis.

During the last two decades, it has been established that mitochondria of eukaryotic cells form a reticular network in most cell types with a few exceptions of e.g. neuronal axons, retina, *etc.* (see e.g. [12]). The network is continuously remodeled by cycles of fission and fusion events, giving rise to various mitochondrial reticulum shapes, ranging from long, branched, and interconnected tubules to solitary sacks or cisternae. The number of tubules, their connections, overall morphology, and subcellular distribution is thus dynamically altered. Consequently, mitochondrial network morphology must be linked to the

Abbreviations: FCCP, carbonylcyanide-*p*-(trifluoromethoxy)phenylhydrazone; mRoGFP, mitochondrial matrix targeted redox-sensitive GFP

* Corresponding author. Tel.: +420 296442760; fax: +420 296442488.
E-mail address: jezek@biomed.cas.cz (P. Ježek).

0005-2728/$ – see front matter © 2008 Published by Elsevier B.V.
doi:10.1016/j.bbabio.2008.04.002

mitochondrial function or state, thus reflecting specific cellular requirements or pathological states.

A new paradigm was set by studies revealing the protein machinery responsible for mitochondrial fusion, fission, (or remodeling) events [13–15], called thereafter mitodynamins. It has been recognized that these processes are highly regulated and depend on the activity of mitochondria. The overall mitochondrial reticulum shape is controlled by the balance between fusion and fission events. Mammalian profusion proteins contain a GTPase domain and involve outer membrane mitofusins MFN1, and 81% homologous MFN2 [16–25] and intermembrane space plus inner membrane OPA1 [25–34]. Outer and inner membrane fusions seem to be separate events: fusion of the outer membrane relies on low levels of GTP hydrolysis, while fusion of the inner membrane requires elevated levels of GTP hydrolysis and depends on the existence of the protonmotive force (Δp), hence ATP synthesis [35]. Loss of either MFN1 or MFN2 is lethal [17]. MFN1-lacking mouse embryonic fibroblasts (MEF) have fragmented mitoreticulum with short tubules and small uniform spheres of the same diameter as tubules, whereas in MEF lacking MFN2, fission leads to various size fragments [17]. This could reflect the finding that MFN1-mediated tethering activity and GTPase activity is higher than those of MFN2 [19], provided that the higher activity is required for sewing greater size objects, whereas lower tethering is required to sew regular objects together. MFN1 seems to act in concert with OPA1, since OPA1 overexpression in MEF lacking MFN1 does not restore fusion, whereas in MEF lacking MFN2 it does [25]. The fusion mechanism for outer membrane likely involves tethering of two membranes by their residing mitofusins and subsequent mechano-chemical action of the GTPase domain or its regulation of other downstream proteins, similar to classical small G proteins. An action of mitochondrial phospholipase D is also involved [22].

OPA1 was reported to promote fusion depending on MFN1 [25,29]. Mutations in OPA1 gene lead to optic athrophy [30]. The OPA1 expression involves an alternative splicing (eight mRNA isoforms [26]), protein proteolytic processing, as well as tissue specific expression [25,27–34]. It leads to number of bound or soluble protein forms, whose specific functions are still unknown. As an example, an assembly of two long and one short (cleaved) form of OPA1 has been found to connect the outer and inner membrane in the cristae outlets and suggested to initiate apoptosis upon tBID-mediated outlet opening enabling cytochrome *c* release [27,29]. Thus OPA1 is also important for maintaining regular cristae structure, which is critical for function of oxidative phosphorylation (OXPHOS) enzymes. It protects cells from apoptosis by restricting the diameter of cristae junctions independently of mitochondrial fusion, thereby preventing cytochrome c release. The significance of low-abundant OPA1 cleavage products for mitochondrial fusion and function, cleaved for example by rhomboid PARL protease [28,29] or by paraplegin [29], is not clear. They may play a role in controlling apoptosis.

The fission machinery includes FIS1 proteins spread evenly on the outer membrane surface [36–40], and a large cytosolic GTPase DRP1 partially associated with the outer membrane [41–44]. After Cdk1/cyclin B-dependent phosphorylation [44] or other unknown stimuli, DRP1 is recruited from the cytosol to the outer mitochondrial membrane where it docks to FIS1 [41,42]. Other pro-fission proteins, such as MTP18 [45], or fatty acyl transferase called Endofilin B1 [46] or GDPAP1 participate probably downstream of DRP1 in the control of mitochondrial fission. Mitofilin was found to be involved in the cristae remodeling [47]. However, the coordination of fission of both membranes remains to be elucidated.

Other novel less elucidated proteins are recognized to interact with mitodynamins. Thus, mitofusin binding protein, MIB [48], and stomatin-like protein 2, STOML2 [49], associate with mitofusins, whereas E3 ubiquitin ligase MARCH-V (RING-CH-V) acts upstream of DRP1 [43]. Moreover, a non-apoptotic role of Bax and Bak has been revealed in regulation of mitochondrial fusion through the punctuate spots in which they interact with MFN2 [24]. In such spots of the outer membrane where Bax and Bak concentrate, also DRP1 and MFN2 colocalize and these foci subsequently become fission sites [16].

The link between OXPHOS and activity of mitodynamins is given by GTP levels as most of the mitodynamins are GTPases. Local cytosolic levels govern DRP1 activity, peri-mitotubular levels mitofusin activity, and levels in the intermembrane space OPA1 activity. The knowledge of upstream modulators of mitochondrial dynamics is still not complete. For example, Ca^{2+} was assumed to modulate the activity of dynamin and regulatory GTPases resulting in mitochondrial morphological alternations, perhaps though regulation of mitochondrial movement along the microtubule scaffold [50]. As indicated above balance between fusion and fission must exist as both processes in their extremes participate in apoptosis [13,14], thus any serious deviation can have harmful effects on cells.

Recently, it has been recognized that not only bioenergetic parameters, respiration, Δp and their components, electron and substrate fluxes, but also an overall morphology or dynamics of mitochondrial network within the living cells may reflect their bioenergetics, and therefore healthy or disease status [51–57]. Analogously to cristae remodeling of Hackenbrock [12], a major correlation reflected OXPHOS status [51,52]. Numerous evidence has been reported showing that mitochondrial morphology is crucially linked to the energy metabolism. A first link is given by the already mentioned GTP requirement for mitodynamins. GTP is produced by the Krebs cycle or from ATP by matrix and cytosolic nucleoside diphosphate kinases. Its export mechanism from the matrix is unknown. Variations in respiration and their feedback to Krebs cycle and also changes in ATP levels might be connected to possible mitochondrial morphology modulators. In general, it seems that undisturbed highly efficient OXPHOS correlates with a highly interconnected, ramified network and enlarged cristae compartments [51,52], whereas low OXPHOS activity and high glycolysis correlate with bulkier or more spherical tubules, or 2D images of apparently solitary mitochondria [51,52] displaying reduced intracristae space. Thus the mitochondrial network with apparently thinner, more branched, and interconnected tubules has been reported when cellular energy substrates were shifted from glycolytic to those allowing predominant OXPHOS [51,52].

Manipulations of expression of mitodynamins lead to morphology changes. For example, MFN2 downregulation in myotubes results in fission combined with simultaneously reduced activity of Krebs cycle and respiratory chain, and enhanced glucose transport, glycolysis and lactic fermentation [18]. MFN2 overexpression led to prevention of high glucose-induced fission [54]. Low levels of DRP1 protein preventing fission [54] have been shown to result in a significantly lower rate of endogenous respiration and thus ATP production, affecting activity of Krebs cycle and OXPHOS and further impacting cell growth and perhaps viability [52]. Also knockdown of mitochondrial phospholipase D results in fission [22].

A rich potential of mitochondrial morphology as a medical diagnostic tool has already been proven. Fragmentation of the mitochondrial network has been observed in fibroblasts from patients with alterations of mitochondrial energy production caused by genetic defects in respiratory chain subunits [53]. Oxygen/glucose deprivation was shown to be related to the DRP1-dependent fragmentation of mitochondrial reticulum [54]. Mitochondrial fission is an early event in ischemic stroke *in vivo* and is also induced by nitric oxide in neurons [58]. Simulations of pathologies can be seen in manipulations of cell energetic status. Thus, when uncouplers like FCCP were added to culture cells for time periods ranging from a minute up to a day, remodeling [41], fragmentation/fission of mitochondrial reticulum [31,32,34,35,59,60], apoptosis [61,62], and changes in gene expression [63,64] were observed. Uncoupler (de-energization) reportedly increases protease-mediated cleavage of

pro-fusion protein OPA1 [29,31–34], whereas valinomycin, respiratory chain inhibitors, and other agents recruit DRP1 from the cytosol [41,52].

A drawback of some of the reported studies can be seen in the fact that they have been conducted with conventional confocal microscope acquiring 2D images. Thus, a mature fission event has been seen as solitary, presumably spherical, mitochondria [31,32,59,60] or a "doughnut-like" shaped mitochondria [51,52]. Frequently no 3D reconstruction was attempted, thus two typical patterns were identified: a thin 2D tubule morphology, correlating with efficiently phosphorylating mitochondria [51,52,65] and a thick 2D tubule morphology observed under glycolytic conditions [51,52] or pathologic conditions [18,53,54]. Even recent reviews still refer to mitochondrial tubules as 500 to 700 nm [13] or ~800 nm diameter objects [57]. To fully understand the mitochondrial network morphology, microscopy techniques, such as 4Pi microscopy [66–74], capable of resolving the 3D nature as well as the small mitochondria tubule diameter of 200–400 nm, have to be applied. This has been impressively demonstrated in yeast (*Saccharomyces cervisiae*) by Egner et al. [74] comparing mitochondria thickness and network branching for growing conditions in glycerol (OXPHOS) and glucose (glycolytic). 4Pi microscopy has also been shown to be feasible in imaging mitochondria in mammalian cells [71].

Here we apply 4Pi microscopy to investigate morphological alterations of mitochondrial networks in a biomedically relevant study of insulinoma INS-1E cells and hepatocellular carcinoma HEP-G2 cells under different cultivation conditions setting distinct autocrine insulin levels in the former and glycolytic states replacing OXPHOS in the latter cells. A striking observation was that in fact predominantly a single mitochondrion, *i.e.* completely interconnected reticulum, exists in cells relying on OXPHOS. Another main feature is that the ~260 nm diameter of tubules was nearly constant along the tubule lengths in intact cells. Situations with less active OXPHOS featured thicker tubules and additional interconnected bulkier cisternae within the reticulum. Moreover, we studied 3D shapes of disintegrated mitochondrial reticulum at rotenone-inhibited respiration or at uncoupling by FCCP. The induced fission cuts either short segments or small spheres with similar tubule diameters as before and disintegrates the original continuous single mitochondrion into several reticula. The increased diameter of tubules or cisternae as well as formation of rings with FCCP suggests that also fusion process was activated. The concomitant ring formation probably results from fusion of short segments. These results argue against inactivation of pro-fusion dynamins such as OPA1 at low or zero Δp and indicate that at low (rotenone) and zero OXPHOS (plus zero Δp, with FCCP) nonzero GTP levels exist, sufficient to drive mitofusin and OPA1 activities. We speculate that namely low-strength tethering MFN2 participates in the mild fusion required to sew segments to rings. A concerted effect of rotenone plus FCCP was found for INS-1E cells where even more intensive fusion acting simultaneously with fission formed bowl-like shapes (shell-like objects or very bulky rings). We hypothesize that in this case also strongly-tethering MFN1 acts to promote fusion into larger objects. In conclusion, we clearly demonstrate that high resolution 3D microscopy techniques such as 4Pi microscopy are required for detailed studies and visualization of mitochondrial network.

2. Materials and methods

2.1. Cell cultivation

The human hepatocellular carcinoma cell line HEP-G2 was purchased from European culture collection (ECACC 85011430). Rat insulinoma INS-1E cells were a kind gift of Prof. Maechler, University of Geneva [75]. The HEP-G2 and INSE-1E cell lines stably expressing matrix targeted redox-sensitive GFP (mRoGFP, the respective vector was a kind gift of Dr. Rossignol, Univ. Bordeaux 2, France; [51]) were cultivated at 37 °C in humidified air with 5% CO_2. HEP-G2-mRoGFP cells were cultivated in DMEM without glucose supplemented with 3 mM glutamine, 5% (v/v) FCS, 10 mM HEPES, 10 IU/ml penicillin, 100 μg/ml streptomycin and 25 mM or 5 mM glucose or 10 mM galactose (in this case glucose-free dialyzed FCS was used). INS-1E-mRoGFP cells were cultivated in RPMI 1640 with L-glutamine, without glucose supplemented with 10 mM HEPES, 1 mM pyruvate, 5% (v/v) FCS, 50 μM mercaptoethanol, 50 IU/ml penicillin, 50 μg/ml streptomycin, 11 mM or 5 mM glucose.

2.2. Sample preparation for 4Pi microscopy

Cells were cultured for 2–4 days to 70% cell confluency on 4Pi quartz coverslips coated with poly-L-lysine. The cells were treated with 1 μM FCCP (Sigma), 20 μM rotenone (Sigma) or both together for 20 min at 37 °C. Then the coverslips were washed two times in 1×PBS buffer. The cells were immediately fixed with 0.3% glutaraldehyde for 10 min at 37 °C. The unreacted aldehydes were reduced by 1 mg/ml sodium borohydride (pH 8) three times for 15 min. Finally, the coverslips were washed three times in 1×PBS. The coverslips with fixed cells were mounted with 87.5% glycerol/PBS mounting medium on the 4Pi metal holders containing coverslips with mirrors and sealed. The fixation protocol was optimized in order to preserve structure of mitochondrial network, which was successfully achieved with the glutaraldehyde treatment. The samples were only imaged by 4Pi microscopy when no differences between conventional confocal 3D images of living cells and the fixed cells could be detected.

2.3. Confocal imaging

A conventional confocal microscopy (Leica TSC SP2) was employed for quality control during sample preparation. Preliminary observations by conventional confocal microscope for all described manipulations (cell cultivation conditions or agent treatments) were performed. 10 to 25 cells on different coverslips were imaged for each conditions. Cells were cultured for 2–4 days on poly-L-lysine coated coverslips to 70% of cell confluency, placed into a thermostable sample chamber supplied by a CO_2 incubator and inspected by the confocal inverted fluorescence microscope Leica TSC SP2, with a PL APO 100×/1.4–0.7 oil immersion objective. An argon laser (488 nm) was used for excitation of mRoGFP. Usually, 20 minute time series (30 min with HEP-G2) of 3D data stacks were recorded, with one 3D stack every 5 min. In the case of rotenone and FCCP treatments, the agents were added after recording the first 3D stack. The resulting change of mitochondrial network structure was observed over time.

2.4. 4Pi microscopy

4Pi microscopy was performed on samples processed in the same way as conventional confocal microscopy (under established conditions or agent treatment) and showed the same morphological results. Data were collected with two Leica TCS 4PI microscopes equipped with pairs of 100×/1.35 NA glycerol immersion objectives. Both systems are set up to operate in Type C mode, using a pair of glass wedges and an optical flat [69], thus achieving an enhanced axial resolution of 100 nm with reduced side maxima. mRoGFP fluorescence was recorded using two-photon excitation at 906 nm wavelength for INS-1E cells and 910 nm for HEP-G2 cells (Chameleon laser, Coherent Laser Group, on both systems) with beam expander 3 or 6 and one photon counting avalanche photodiodes of the system (short pass SP700, band passes 525/50; Chroma Technology Corp.). The pinhole was set to 1 "Airy unit". The objective correction collars, focus alignment and the interference phase of the microscope were adjusted for each individual sample put in the system. The embedding medium, in this case 87.5% glycerol/PBS, was also used as the immersion medium to ensure continuity in the refractive index (n_D ~ 1.46). Stacks of xz images were recorded with a *y* distance between neighboring slices of 31 nm and 61 nm to 122 nm for INS-1E cells and HEP-G2 cells, respectively. The pixel size in each xz image was chosen between 31 nm×31 nm and 36 nm×36 nm (or 56 nm×56 nm) for INS-1E cells and HEP-G2 cells, respectively. Stack dimensions were adapted to the cell size and ranged between 8 and 28 μm for each direction; typical values were 15 μm. In data post-processing, each stack was smoothed and 3-point deconvolved with the LCS software (Leica Microsystems). Typically four cells were imaged by 4Pi microscopy for each conditions. Since the same general features could be observed in all data stacks belonging to the same condition, the figures show only representative single 3D images.

2.5. 3D image analysis

The diameter of mitochondrial tubules was determined from the original measured data stacks by two methods, referred further as "PST" and "ruler" method, respectively. The PST method employed analysis of minima and maxima of the axial intensity profile [74] through at least ten objects which were confirmed as tubules, e.g. they were present in several subsequent frames of a data stack. Objects with extremely large diameters are excluded by this method as they do not provide a proper point-spread function. The ruler method simply measured at least 70 diameters using profile quantification tool of the Leica software on the raw xz data stacks. Also in this case larger objects potentially representing rings, large cisternae, or spheres were excluded from this analysis. For the representation of the distribution of diameters variance plots are shown (Figs. 7–9). 3D projections were created with Amira 4.1.1 (Mercury, Germany) in isosurface mode. The intensity threshold for surface rendering was set to

35 (17 for HEP-G2 cells) to obtain comparable tubule diameters as determined by the PST method and ruler method. This isosurface computation threshold allowed reconstruction of the entire relevant signal but excluded background signal of our data. Figures such as Fig. 5 with color coding of separate objects were employed to count the numbers of each object types. These projections were made using Paraview (Sandia Corporation, Kitware Inc., NM, USA). The threshold setting for isosurface 73 was selected among series of various isosurface thresholds to obtain diameters identical to those obtained from point-spread functions. This software was also used to calculate voxel numbers. This number was converted to obtain a volume of the tubular system by multiplication with the volume of a single voxel (unit picoliters).

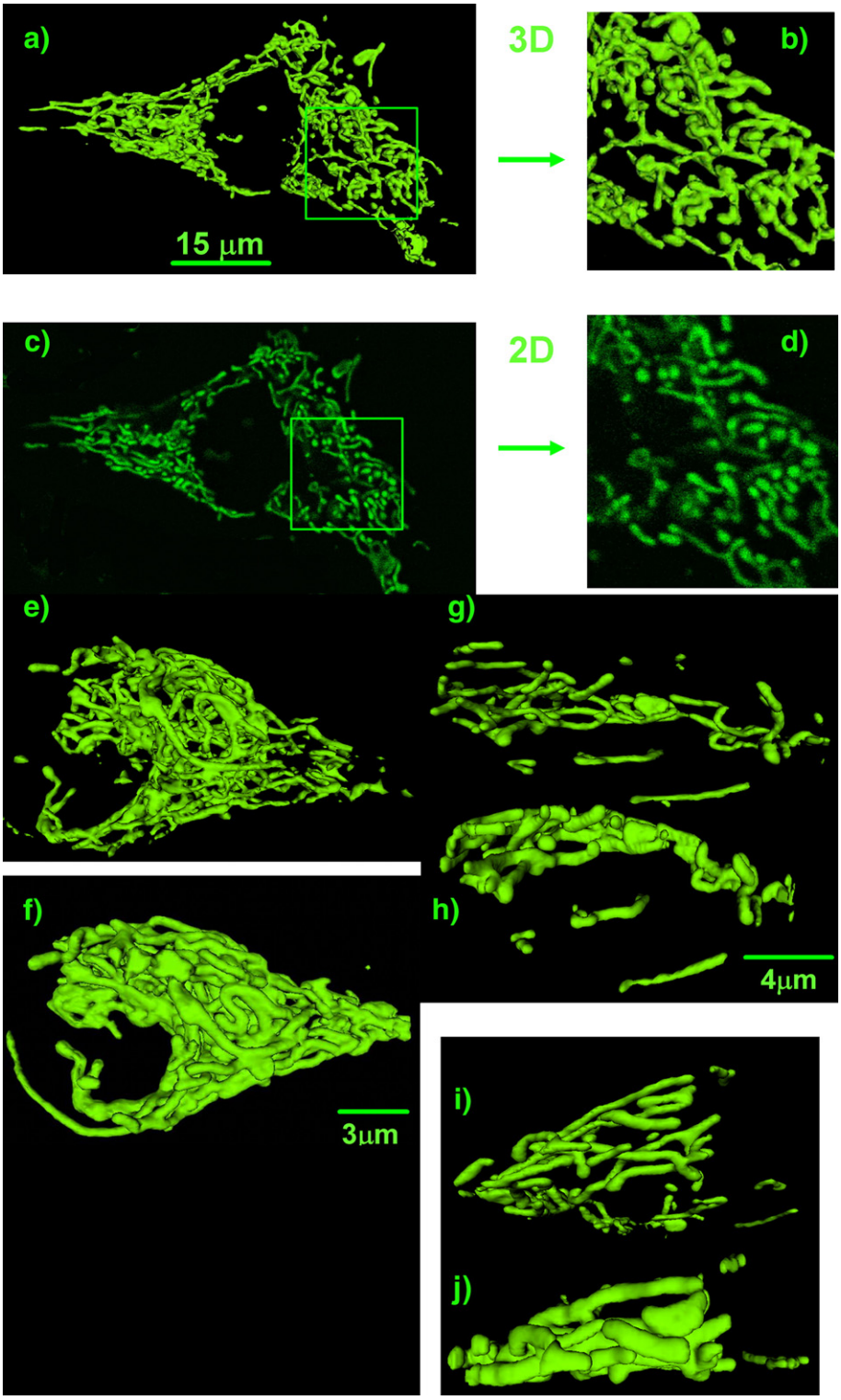

Fig. 1. Comparison of 3D 4Pi microscopy *vs.* 2D imaging and conventional (two-photon) confocal microscopy. Panels a–d illustrate the inability of 2D imaging (c–d) to distinguish, whether an apparent spherical object in the 2D image is not a simply tubular one oriented perpendicular to the image as resolvable by 3D microscopy (a–b). Images a–d show mRoGFP-transfected HEP-G2 cells cultivated in 25 mM glucose recorded by two-photon excitation with a confocal microscope (Leica TCS SP2). Please note that there are seemingly less objects in the 2D image d) than in the 3D image b). Panels e–j compare data recorded with 4Pi microscopy (e, g, i) *vs.* conventional confocal microscopy (f, h, j) on the same Leica TCS 4PI instrument using two-photon excitation. Images show mRoGFP-transfected INS-1E cells cultivated in 11 mM glucose (e, f) and two different areas of a HEP-G2 cell cultivated in 5 mM glucose (g to j) taken from the same sample. The scale in c is equal to a; in e is equal to f; and in i, j is equal to g, h.

3. Results and discussion

3.1. Imaging of mitochondria by 4Pi microscopy vs. conventional confocal microscopy

Imaging of the mitochondrial network morphology by conventional light microscopy, including confocal microscopy, represents a major technical challenge: complex 3D features of the networks cannot be resolved because of the >500 nm depth resolution of these techniques. Other imaging techniques used so far, such as electron tomography [11] and electron microscopy, provide the required resolution, but suffer from complicated sample preparation, which may disturb a natural 3D structure of mitochondrial network, and are limited in the maximum sample thickness to typically less than 1 μm. For the non-invasive 3D visualization of mitochondrial networks, *i.e.* 100–400 nm structures, high resolution 3D light microscopy techniques such as 4Pi microscopy are necessary. The z-axial resolution of a 4Pi microscope reaches 100 nm compared to 500–800 nm of a conventional confocal microscope, thus providing the required resolution to resolve tiny cellular structures in three dimension *in situ*. This resolution is surpassed currently only by STED and related RESOLFT techniques or FPALM, PALM, STORM, and PALMIRA microscopy [75–82], which only recently have demonstrated 3D imaging capabilities but have not been applied to tackle 3D biological questions yet. 4Pi microscopy on the other hand has successfully been demonstrated to resolve, among other structures, microtubules, mitochondria, Golgi apparatus and histone distributions in the cell nucleus at an unprecedented level of detail in 3D [69–74,83]. This technique therefore represents currently the best-tested method to investigate the 3D morphology of mitochondrial networks.

The only disadvantage of state-of-the-art 4Pi microscopy lies in its relatively slow 3D scanning and in an incompatibility of the currently employed sealed coverslip holders and glycerol objectives with imaging of living cells (we have found that the glycerol milieu sets an osmotic shock to the cells and practical oxygen insolubility in 85% glycerol obscures cell respiration). Therefore, we restrained ourselves to imaging of fixed cells.

The described obstacles may stand for the reason why scientists still use 2D mitochondrial imaging, even if fast-scanning confocal

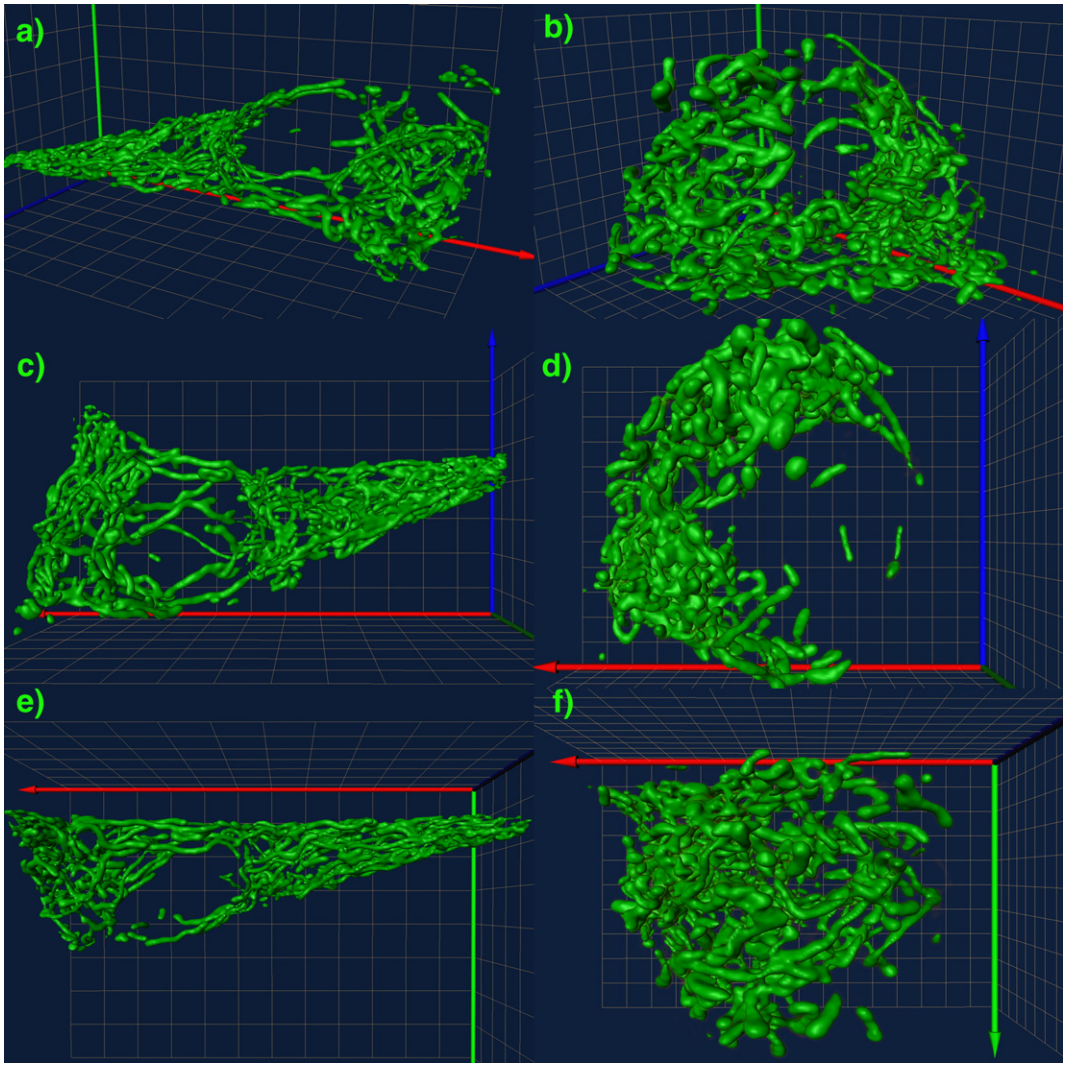

Fig. 2. 4Pi imaging of mitochondrial network in mRoGFP-transfected INS-1E cells. Panels a), c), and e) illustrate INS-1E cells cultivated at 11 mM glucose, representing optimum conditions, while panels b), d), and f) show cells cultivated at 5 mM glucose, *i.e.* lacking autocrine insulin and thus simulating a pathological state. The same cell for each cultivation is displayed in XYZ views in panels a) and b), while in XY views in panels c) and d), and in XZ views in panels e) and f). Color coding for axes: green — *Z* axis; red — *X* axis; blue — *Y* axis. A 1 μm 3D grid is shown in the background. 3D projections were created with Amira 4.1.1. The following parameters were derived for the displayed cells: the intact INS-1E cell cultivated at 11 mM glucose (a), c), e)) shows a dominant single morphological unit of 0.1 pl volume, the average tubule diameter 275±42 nm (PST method, 20 estimates) or 259±37 nm (ruler method, 140 estimates), 85 branching points were recognized within the reticulum as well as over 110 bends; the immature INS-1E cell cultivated at 5 mM glucose (b), d), f)) shows again a dominant single morphological unit, with integrated 36 flat cisternae encompassing the opposite half of the cell, the average diameter was 302±30 nm (PST method, 10 estimates) or 310±36 nm (ruler method, 70 estimates), 45 branching points were recognized within the reticulum as well as over 65 bends.

microscopes enabling 3D imaging are available. However, here we demonstrate that the 2D imaging of mitochondrial network is not sufficient, since it cannot distinguish, whether an apparent spherical object in a 2D image is not just a tubule oriented vertically (Fig. 1a–d). 3D scans are required to assess this distinction, even at a resolution lower than that of the 4Pi microscope (Fig. 1c, d). For small cells such as insulinoma cells (INS-1E) featuring dense, branched tubular mitochondrial reticulum, these tubular structures are however hardly separable in conventional confocal microscopy images. Due to the lower resolution, 3D conventional or two-photon excitation confocal scanning always shows thick tubules or objects in the images, as shown in Fig. 1e–j. As a result, 4Pi microscopy yields currently the highest fidelity high resolution 3D images of mitochondrial network (Figs. 1–7; Movies I to VII of Supplemental information).

Such a highly dense network of mitochondrial reticulum is illustrated for insulinoma INS-1E cell line in Fig. 2 (see also Movies I to V of Supplemental information). When cultivated at optimum 11 mM glucose INS-1E cells secrete autocrine insulin and exhibit nearly maximum OXPHOS [75,84]. Therefore these cells represent an excellent example of OXPHOS type cells. The observed rich mitochondrial network fills the whole cell and comprises of thin infrequently branched mitochondrial tubules. These are hardly distinguishable by conventional confocal microscopy, where their diameters appear to be two to four times higher in axial direction (Fig. 7a). Mitochondrial tubules are very close to each other. In certain parts of the cell, such as in the cell tip, one cannot resolve mitochondrial network. The major feature of their network can be seen in the fact that in most cases only one dense very large continuous network accompanied by only a few small objects is recognized. This means that in these cells predominantly one large mitochondrion exists forming a single mitochondrial reticulum (Fig. 2a, c, e; Movie I under Supplemental information). Random fission events probably led to the observations of a few small additional objects such as small spheres in each cell. In all five completely evaluated cells one large reticulum was found.

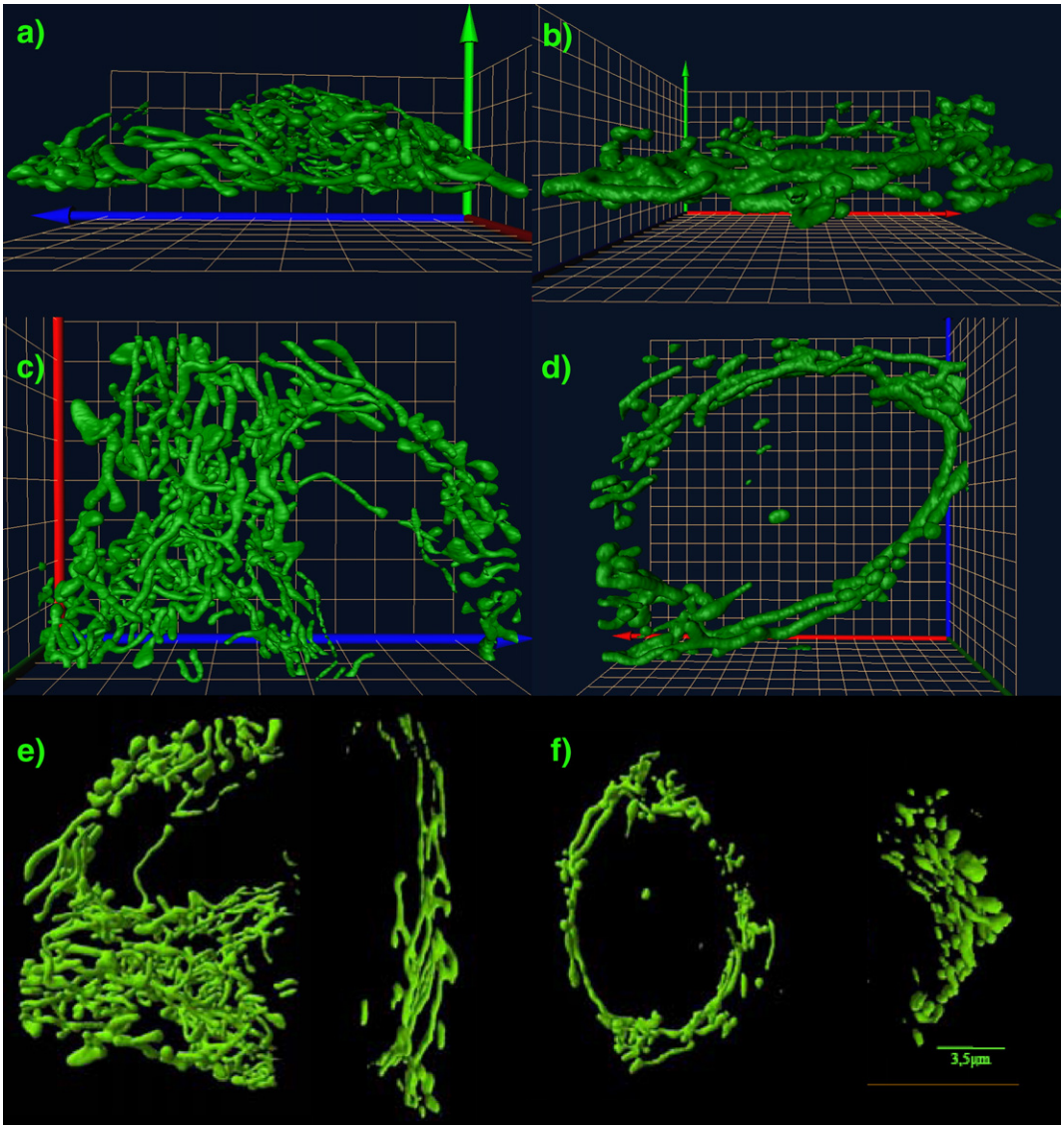

Fig. 3. 4Pi imaging of mitochondrial network in mRoGFP-transfected HEP-G2 cells. Panels a), c), and e) illustrate HEP-G2 cells cultivated at 5 mM glucose, representing optimum conditions, while panels b), d), and f) show cells cultivated at 25 mM glucose, *i.e.* hyperglycaemic conditions with dominant glycolysis. Color coding of axes and grid size are identical to Fig. 1. 3D projections were created with Amira 4.1.1. Panels e) and f) show XY views of the same cell for each cultivation as shown in panels a) to d) and details of the different second cell for each cultivation. The following parameters were derived for the displayed cells: the intact HEP-G2 cell (a), c), e)) cultivated at 5 mM glucose shows a dominant single morphological unit and three smaller fragments with 14 integrated flat cisternae plus four separate small spheres and five short tubules. The average tubule diameter was 302 ± 40 nm (PST method, 10 estimates) or 277 ± 53 nm (ruler method, 70 estimates). It included 35 branching points and over 50 bends. The hyperglycaemic HEP-G2 cell (b), d), f)) shows one main morphological unit plus six short segments, six cisternae are integrated within the tubular reticulum. The average diameter was 445 ± 128 nm (PST method, 7 estimates) or 355 ± 100 nm (ruler method, 40 estimates). It included 22 branching points and 20 bends.

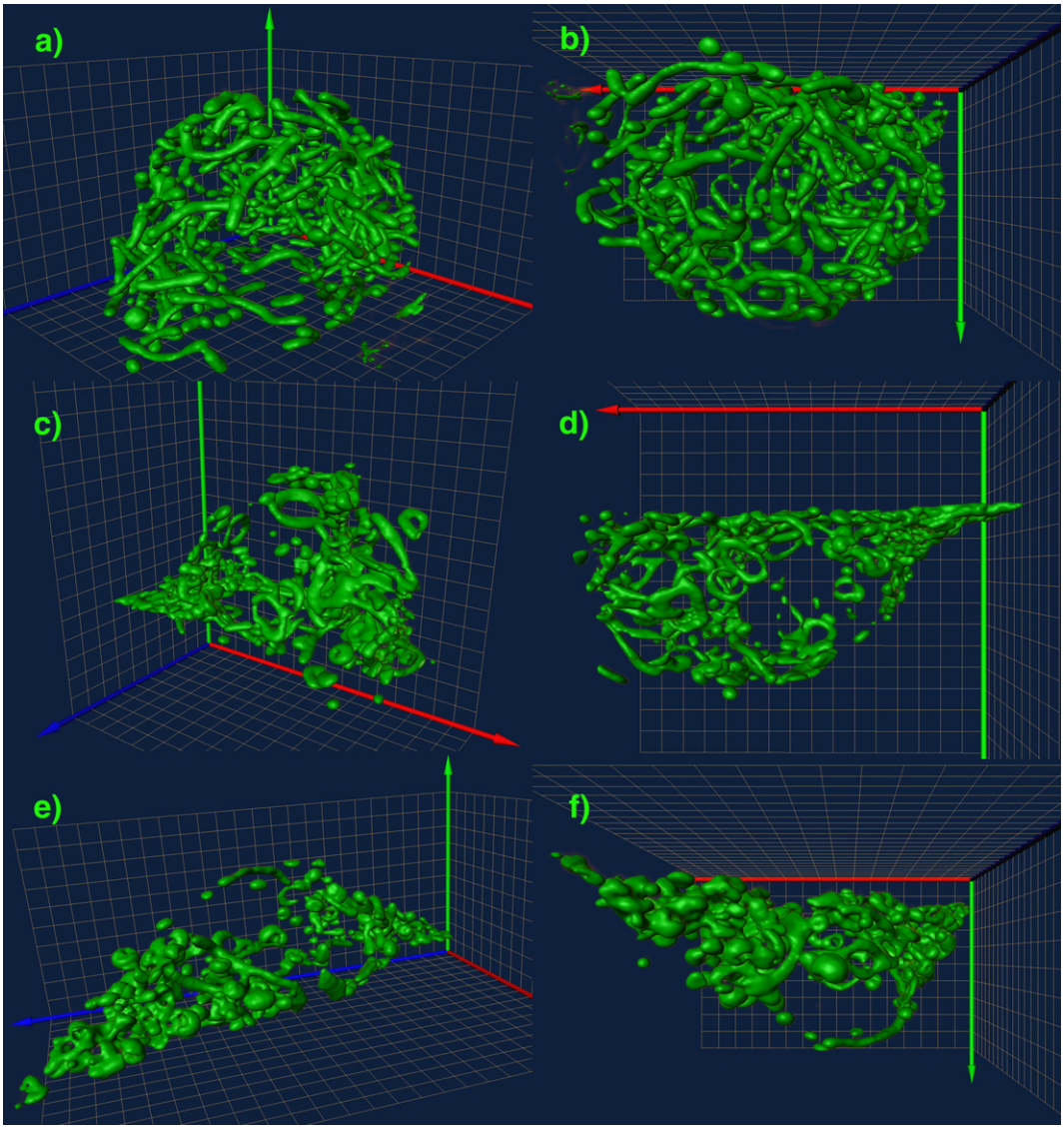

Fig. 4. 4Pi imaging of disintegration of mitochondrial network in INS-1E cells. Disintegration of originally highly interconnected mitochondrial reticulum in INS-1E cells upon addition of 20 μM rotenone (panels a) and b)), 1 μM FCCP (panels c) and d)), and both these agents (panels e) and f)) is shown for the same cell in each treatment in XYZ (left panels) and XZ views (right panels). Color coding of axes and grid size are identical to Fig. 2. 3D projections were created with Amira 4.1.1. The following parameters were derived for the displayed cells: Rotenone-treated sample (panels a) and b)): 40 separate morphological units (see Fig. 5a) filling a volume of 0.05 pl, among them seven fractions of the original large mitochondrial reticulum, 15 spheres, and 18 short segments. The average tubule diameter was 351 ± 23 nm (PST method, 9 estimates) or 330 ± 48 nm (ruler method, 70 estimates). Only 8 branching points were detected. FCCP-treated sample (panels c) and d)): 45 morphological units (see Fig. 5b) encompassing a volume of 0.04 pl, among them four clusters of long interconnected tubules, 23 spheres, 15 short segments, three separated rings, and seven integrated rings and 24 integrated cisternae. The average tubule/object diameter was 305 ± 19 nm (PST method, 10 estimates) or 290 ± 53 nm (ruler method, 70 estimates). Altogether, 25 branching points were recognized. FCCP and rotenone-treated sample (panels e) and f)): 35 morphological units (see Fig. 5c) extended in a volume of 0.045 pl, among them four clusters of long interconnected tubules including 10 branching points, 18 spheres, four short segments, eight integrated rings, and nine integrated and nine separate vessels, or shell-like structures appearing as bottom-closed rings; the average tubule/object diameter was 322 ± 36 nm (PST method, 10 estimates) or 304 ± 46 nm (ruler method, 70 estimates).

Additionally, up to ten small morphological units (up to five small spheres and zero to eight short segments) were recognized. The mitoreticulum volume of a typical big cell (Fig. 2a) was 0.1 pl (0.03 to 0.1 pl in all studied cells, Table 1). 65 to 85 branching points and more than 50, in a few cases more than 100, bends of mitochondrial tubules could be observed per cell. At 20 to 30 locations per cell the tubules were transferred or the two neighboring tubules were fused in bifurcation points into flat objects, thereafter called cisternae, usually with a ~200 nm × 400–600 nm profile of various length up to 1 μm. A striking feature of the single mitochondrion in INS-1E cells lies in the fact that a nearly constant tubule diameter within the overall topology (neglecting the cisternae) and infrequent branching was observed (Figs. 2a, c, e and 7a, b, c; Table 1). The average tubule diameter of ten cells evaluated by the PST method was 270 ± 28 nm (the average of the best five images with ideal point-spread functions was 262 ± 26 nm — see Fig. 7b, Table 1). These values were at the detection limit of our analysis defined by the resolution of 4Pi microscopy. The actual, "true" diameter of mitochondrial tubules in INS-1E might be even smaller.

3.2. Mitochondrial network morphology in INS-1E cells as reflection of autocrine status

A slightly different situation was found with INS-1E cells cultivated at low 5 mM glucose (Fig. 2b, d, f; Movie II of Supplemental information, Fig. 7b, Table 1). Since INS-1E cells require glucose and autocrine insulin is essential for their optimum growth [75,84], the decreased glucose led to three-fold longer doubling time and impaired secretion of insulin upon glucose stimulus [75,84]. Cells also loose

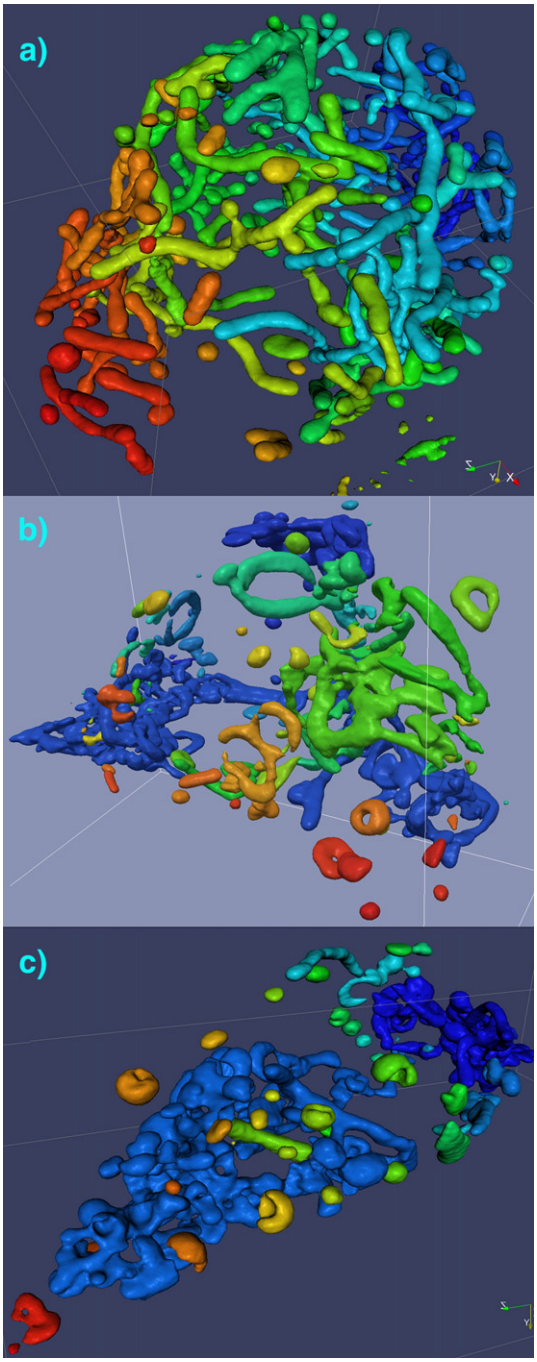

Fig. 5. Color coding of individual objects in 4Pi images of mitochondrial network disintegration in INS-1E cells. Disintegration of originally highly interconnected mitochondrial reticulum in INS-1E cells upon addition of 20 μM rotenone (panel a)), 1 μM FCCP (panels b)), and both these agents (panels c)) is represented by color coding of images shown in Fig. 4a), c), e), respectively. 3D projections were created with Paraview.

their conical shape and are mostly round–oval. Their tubules exhibited an average diameter increased by ~40 nm (Fig. 7b, Table 1). In 40 to 50 locations tubules or their branching or bifurcation points were transferred into flat cisternae and in some cells accompanied by up to 100 much smaller flat cisternae. The increase in number of cisternae was characteristic for these immature INS-1E cells and indicates a shift of fusion/fission equilibrium toward fusion. Nearly all objects, tubules and cisternae appeared interconnected at 100 nm of the 4Pi microscope (gaps smaller than 100 nm cannot be excluded). Again in all four evaluated cells, one main reticulum was observed plus one to six small ~300 nm spheres and one to six short tubular segments. The number of branching decreased to 40 to 60. Some cells contained tubular structures in half of the cell volume, while cisternae dominated the opposite halves (Fig. 2b, d, f).

The exposure of INS-1E cells cultivated at 11 mM glucose to high 25 mM glucose concentration caused only slight periodical changes in tubular thickness without any sustaining fragmentation. Thus after 20 min of cell incubation, 4Pi microscopy did show only a ~15 nm increases in the mean tubule diameter (Fig. 7b, c, Table 1). Otherwise, the mitoreticulum maintained branching and other characteristics.

3.3. Mitochondrial network morphology in HEP-G2 cells as reflection of oxidative phosphorylation

The opposite case to the OXPHOS cell type can be seen in glycolytic cells, surviving on glycolysis with more or less active OXPHOS. Most of the cultured cells with exception to primary cultures belong in this group since they are fused to cancer cells to be immortalized. Moreover, it has been shown that mitochondrial morphology depends on cultivation conditions that lead to different OXPHOS intensity, as first described by Rossignol et al. in HeLa cells [51]. A “thin type” of mitochondrial reticulum was observed in cells relying on OXPHOS (cultivated in galactose/glutamine), a “thick type” in cells cultivated at high glucose. We confirmed these observations also with HEP-G2 cells (not shown).

Using 4Pi imaging we now show detail 3D images of these two typical types of mitochondrial reticulum while manipulating only glucose concentration during cultivation of HEP-G2 cells. At low 5 mM glucose HEP-G2 cells have dense, slightly branched tubular mitochondrial network (Fig. 3a, c, e, and Movie VI of Supplemental information; since the HEP-G2 cells are three to four-fold larger than INS-1E, only parts of cells could be imaged). In the scanned regions (typically 30–50% of the complete cell) of four cells the network comprised of one to 12 separate units dominated by one large reticulum and up to two small or medium-sized reticula and remaining one to eight short tubules (Fig. 3a, c, e; see also Movie VI of Supplemental information). The tubule diameter average was 20 nm higher than in INS1 cells (Fig. 8a, b, Table 1). Branching frequency of the reticulum was significantly lower than in INS-1E cells (13 to 35 branches per scanned volume). At more than 25 locations tubules were transformed into flat cisternae. Perhaps due to the larger size of HEP-G2 cells, less bends were recognized (~50). In contrast, mitochondrial morphology patterns with bulkier mitochondrial networks were observed at high, 25 mM, glucose level, mimicking chronical hyperglycemia (Figs. 3b, d, f and 8a, b; Movie VII of Supplemental information). Mitochondrial tubules or bulky cisternae showed 100 larger diameter (Fig. 8a, b, Table 1). This increase corresponds to switch of energy metabolism to cytoplasmic glycolysis at low rate of mitochondrial OXPHOS. The reticulum is located mainly perinuclearly with numerous bulky spherical cisternae in the distal cellular regions (Fig. 3f). These morphological patterns are similar to those described by Yu et. al. [54], who observed, that mitochondria of rat hepatocytes and myoblasts undergo rapid fragmentation upon exposure to high glucose.

3.4. Disintegration of mitochondrial network at inhibited respiration

We further investigated whether decreasing OXPHOS at substantially inhibited respiration (down to 20% to 10%) by rotenone is reflected by changes in mitochondrial network morphology. A mild oxidative stress is established under these conditions [85], however, other evidences (see below) support that it is rather a respiratory inhibition than the oxidative stress that initiates morphological changes under these conditions. The first treatment was induced by rotenone for a period of 20 to 30 min. Figs. 4a, b and 6a, b show typical resulting morphology changes of mitochondrial networks in their final stages in INS-1E cells (see also Movie III of Supplemental information) and HEP-G2 cells, respectively. The images reflect fission events disintegrating original entirely connected mitochondrial networks. In INS-1E cells, the single

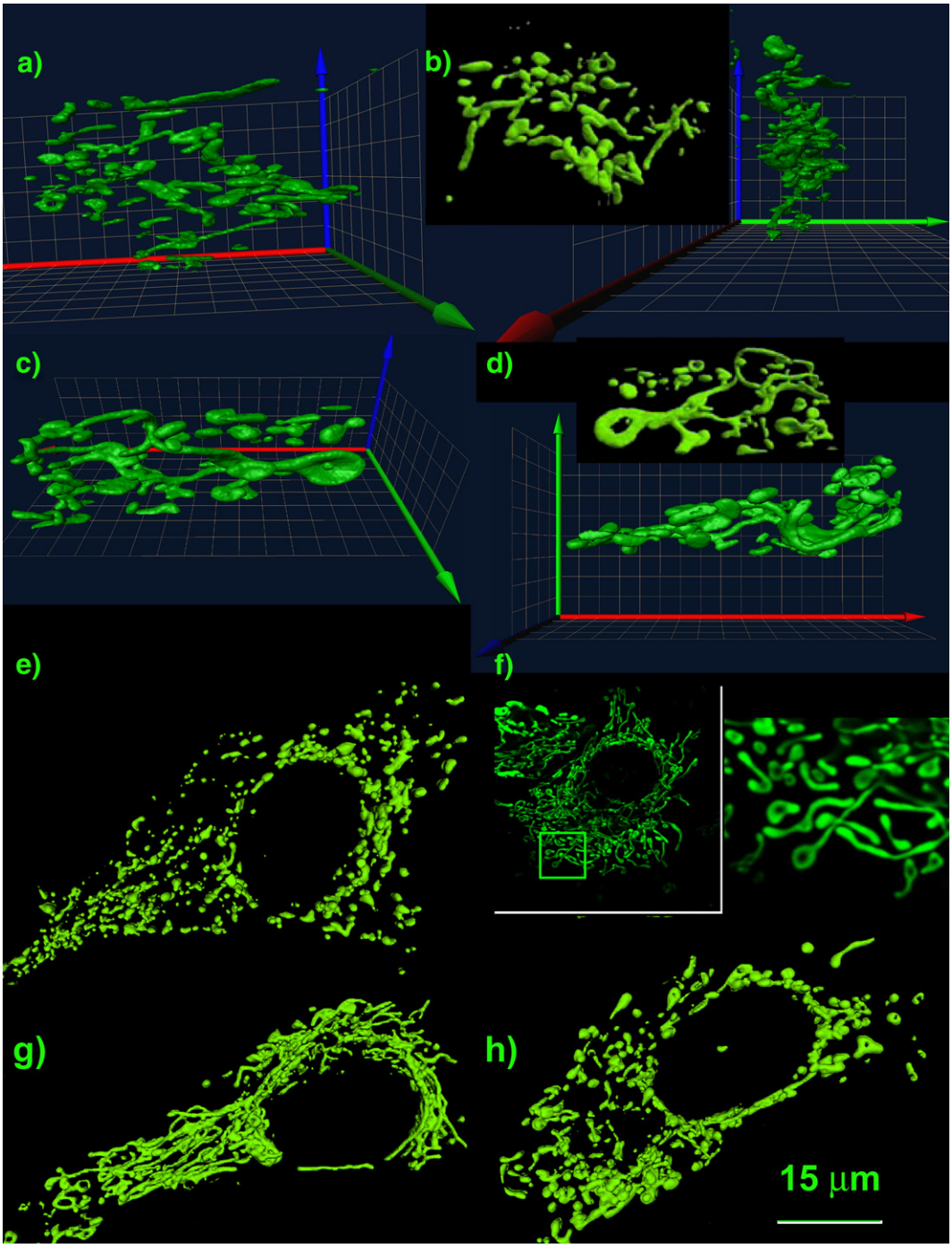

Fig. 6. 4Pi imaging of disintegration of mitochondrial network in HEP-G2 cells. Disintegration of originally highly interconnected mitochondrial reticulum in HEP-G2 cells upon addition of 10 μM rotenone (panels a, b, and e), 1 μM FCCP (panels c, d, f, and h), and both these agents (panel g) is shown in various projections created with Amira 4.1.1. as imaged by 4Pi microscopy (panels a)–d), including insets; color coding of axes and grid size are identical to Fig. 2); and by conventional confocal microscopy (panels e)–h). In all cases HEP-G2 cells were cultivated at 5 mM glucose before treatment. The following parameters were derived for the displayed cells: Rotenone-treated sample (panels a, b, and e): more than 20 morphological units, among them five fragments of reticulum with 15 flat cisternae and 15 short segments; the average tubule diameter was 354±26 nm (PST method, 9 estimates) or 324±46 nm (ruler method, 60 estimates). FCCP-treated sample (panels c, d, f, and h): 32 morphological units, among them a single main reticulum, 16 spheres, 13 short segments, 8 integrated, two separate and six integrate bottom-closed rings; the average tubule/object diameter was 312±65 nm (PST method, 8 estimates) or 258±44 nm (ruler method, 50 estimates); the reticulum included 13 branching points.

mitoreticulum desintegrated into either seven main reticula or one major reticulum plus two to seven small ones; and into an additional 15 to 40 small objects (n=4) (e.g. Fig. 5a). We could observe two types of objects literally cut from the reticula and reshaped into ~300 nm spheres (seven to 19) or shorter segments of tubules of unchanged, *i.e.* ~300 nm, diameter (eight to 21). The number of branching points decreased to 10 or stayed constant. The average tubule (object) diameters rose by 60 and 54 nm, in INS-1E and HEP-G2 cells (Figs. 9 a, b and 8a, b) respectively (see also Table 1). The observed disintegration of mitochondrial networks corresponds to results of Benard et. al. [52] with the exception of their observation of doughnut-shaped mitochondria as the final stage of rotenone treatment. Cells treated for 72 h with rotenone were reported to increase mitochondrial branching (not in our case) and complexity, while the number of mitochondria per cell and cellular ROS levels were

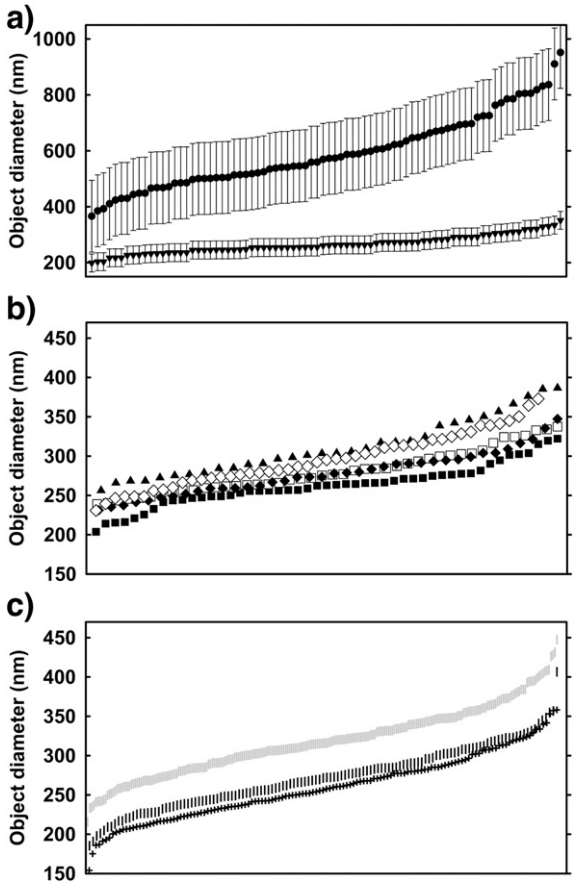

Fig. 7. Charts of tubule diameter variance for INS-1E cells. a) comparison of 4Pi microscopy *vs.* conventional (two-photon) confocal microscopy for INS-1E cells cultivated at 11 mM glucose. The data of four cells were evaluated by the ruler method for variance of tubules diameters in INS-1E cells cultivated at 11 mM glucose as imaged by the Leica TCS 4PI microscope (triangles) or the same cells in the conventional confocal mode of the same instrument (circles). b), c) comparison of INS-1E cells cultivated at 11 mM glucose, 5 mM glucose, and with added 25 mM glucose. b) PST method: The data of five cells (10 estimates for each) were evaluated for INS-1E cells cultivated at 11 mM glucose as measured on the 1st instrument (at The Jackson Laboratory, black squares) or the 2nd instrument (at Leica Microsystems, Mannheim, Germany, open squares); for cells to which glucose was added to the final 25 mM concentration for 20 min (closed and open diamonds for the 1st and 2nd instrument, respectively), and immature cells cultivated at 5 mM glucose (triangles). Diameters were derived from point-spread functions of the measured original data stacks analyzing minima and maxima of the axial intensity profile through tubules (PST method, see Ref. [74]). c) Ruler method: The data of ten cells (70 estimates for each) were evaluated for INS-1E cells cultivated at 11 mM glucose (crosses), with added glucose to final 25 mM concentration (bars); and cultivated at 5 mM glucose (grey bars). Points in variance distribution represent averages within a "channel of magnitudes" of five cells. Cells were imaged on both instruments.

not affected by this treatment [53]. Possible explanations involve obvious reasons such as the use of different cell lines as well as different concentration and times of rotenone treatment but it could also be the result of the lower microscope resolution used in the past. Note that the rightmost 3D projection of 4Pi microscopy data as displayed in Fig. 6b, shows, if viewed in 2D a similar image as obtained by the conventional confocal microscope (see e.g. Fig. 6e).

We conclude that at the Complex I respiratory inhibition, lowering substantially OXPHOS and hence ATP export to the cytosol, the fission/fusion equilibrium is obviously shifted to fission, perhaps due to DRP1 activation. With an antioxidant, mitochondria-targeted quinone, MitoQ, that prevents the rotenone-induced oxidative stress (Plecitá-Hlavatá et al., unpublished), similar morphology changes were observed. Moreover, KCN, which inhibits mitochondrial respiration completely, caused also disintegration of mitochondrial network (not shown). Consequently, the cause for the increased fission frequency was therefore most likely de-energization due to respiratory inhibition and not the mild oxidative stress.

3.5. Disintegration of mitochondrial network due to uncoupling

We have further studied effects of de-energization of mitochondria caused by uncoupling, which sets a zero protonmotive force (Δp; and nearly zero membrane potential and zero OXPHOS). Uncoupler-induced changes in mitochondrial network morphology have been reported already in the pioneer observations [31,32,34,35,41,59,60]. Conventional confocal 2D images showed uncoupler-induced changes as a complete mitochondrial network disintegration resulting in numerous small circular spots, which were interpreted to be small spherical solitary mitochondria [31,32,34,35,41,59,60] or doughnut-like shapes [51,52]. In case of our two cell lines we now reveal much subtle fission by 4Pi microscopy (Figs. 4c, d, 5b, 6c, d, 8a, b, 9a, b, Table 1) as compared to conventional confocal microscopy (Figs. 4e and 6f, h).

For INS-1E cells treated with FCCP the single mitoreticulum disintegrated into two to six main reticula. The number of small morphological units increased to 20 to 40 (n=3) (e.g. Fig. 5b). The solitary circles observed in 2D can be explained to some degree by small ~300 nm spheres found also by 4Pi microscopy (8 to 23 per cell, n=3). Another fraction could result from projections of short, maximum 2 μm segments of unchanged (~300 nm) diameter (9 to 15 per cell, n=3) oriented predominantly in the z-direction. Larger spots observed in 2D may result from projections of ~1 μm bulky spherical or flat cisternae (16 to 24 per cell, n=3) found by 4Pi microscopy. The doughnut shapes previously observed in 2D are confirmed by ~700–2000 nm diameter rings imaged by high resolution 3D 4Pi microscopy. Since they show unchanged tubule diameters compared to the orginal tubules, they are probably formed by fused short tubule segments. In the three completely evaluated whole cells, five to eight rings integrated within the reticulum and two to three separate rings were found per cell. Formation of rings appears to be a hallmark of the

Table 1
Diameters of tubules or other objects and volumes of whole mitochondrial network

Cells cultivation, treatment	Diameter (PST method) (nm)	Diameter (ruler method) (nm)	Mitochondrial network volume (pl)
Insulinoma INS-1E cells			
11 mM glucose			
1st instr.	262±26 nm (5)	245±42 nm (5)	0.09; 0.034
2nd instr.	280±27 nm (5)	270±38 nm (5)	0.038
All data	270±28 nm (10)	266±39 nm (10)	–
25 mM glucose			
1st instr.	277±27 nm (4)	269±40 nm (4)	0.028
2nd instr.	295±34 nm (6)	261±37 nm (6)	0.10; 0.05
All data	287±32 nm (10)	259±41 nm (10)	–
5 mM glucose, 1st instr.	311±36 nm (4)	313±43 nm (4)	0.038; 0.043; 0.035; 0.039
11 mM glucose, rotenone	330±34 nm (4)	308±50 nm (4)	0.037; 0.038; 0.049
11 mM glucose, FCCP	289±25 nm (3)	283±45 nm (3)	0.027; 0.037; 0.043
11 mM glucose, rotenone and FCCP	303±30 nm (3)	287±47 nm (3)	0.032; 0.037; 0.046
Hepatocellular carcinoma HEP-G2 cells			
5 mM glucose	284±38 nm (4)	265±50 nm (4)	0.035*
25 mM glucose	417±107 nm (5)	338±68 nm (5)	n.d.
5 mM glucose, rotenone	338±56 nm (2)	310±50 nm (2)	n.d.
5 mM glucose, FCCP	311±60 nm (2)	279±58 nm (2)	n.d.

Diameters and volumes evaluated as described in Materials and methods are listed for imaging by two instruments ("1st instr." at The Jackson Laboratory; "2nd instr." at Leica Microsystems, Mannheim, Germany). Numbers of imaged cells are indicated in parentheses. A typical number of diameter estimates was 10 for PST method and 70 for ruler method. Note, * points out to the fact that not the whole cell was imaged, but the same spatial region as for INS-1E cells.

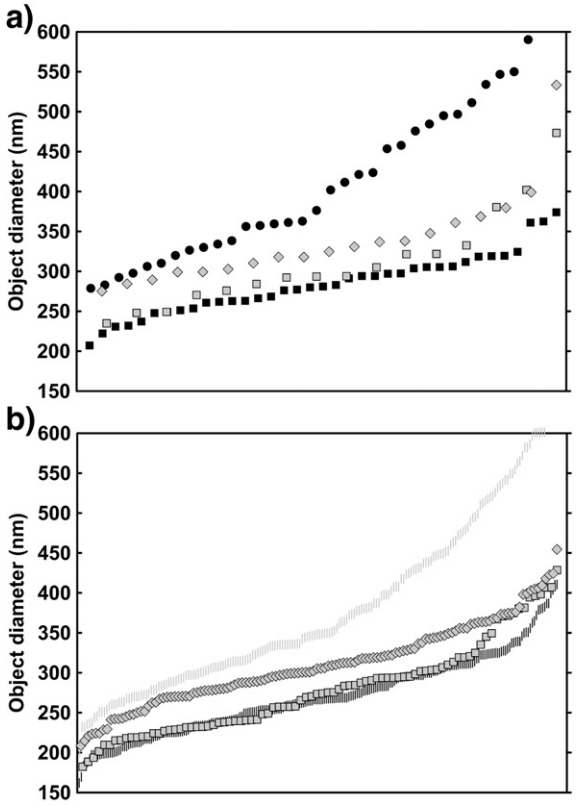

Fig. 8. Charts of tubule diameter/object size variance for HEP-G2 cells. a) PST method: The data of four and five cells (7 to 10 estimates for each) were evaluated for HEP-G2 cells cultivated at 5 mM glucose (black squares) and 25 mM glucose (black circles), respectively, and of two cells (7 to 10 estimates for each) cultivated at 5 mM glucose and treated with 1 μM FCCP (grey squares) or 20 μM rotenone (grey diamonds) for 30 min; measured on the 2nd instrument (see Fig. 7 legend). b) Ruler method: The data of five cells (50 to 60 estimates for each) were evaluated for HEP-G2 cells cultivated at 5 mM glucose (black bars), 25 mM glucose (grey bars), and at 5 mM glucose treated with 1 μM FCCP (grey squares) or 20 μM rotenone (grey diamonds) for 30 min. Points in variance distribution represent all data.

uncoupler-induced changes in INS-1E cells (Figs. 4c, d and 5b; Movie IV of Supplemental information). The average tubule (object) diameter slightly increased by ~20 nm (Fig. 9a, b, Table 1). Note, however, this variance does not include large cisternae or rings. The number of branching points decreased to 15 to 25 per cell.

In conclusion, FCCP induced a morphological pattern composed of four types of units instead of a practically single mitochondrion found in intact INS-1E cells. Besides the remaining single or a few portions of the original single mitoreticulum, short tubules and spheres of the same diameter as reticulum tubules, as well as rings formed most probably by fused short tubules of equal diameter were observed. The established morphology of rings probably results from an imbalance of fission/fusion equilibrium so that fission at collapsed Δp occurs initially in two points 2 to 6 μm apart on tubule and either the resulting short segment remains or is fused into a ring. Certain tubules are fused into cisternae. The rings or new cisternae may hypothetically arise from the elevated fusion due to a local increase in GTP concentration and concomitant activation of mitodynamin GTPases, since faster uncoupled respiration accelerates GTP formation within the Krebs cycle and the sudden lack of matrix ATP might lead to GTP export via the ADP/ATP carrier. We may even speculate that despite the reported cleavage of a subset of pro-fusion OPA1 isoforms into an inactive short form [31–34], other OPA1 isoforms in concert with other pro-fusion mitodynamins help to fuse the segments into the rings or cisternae. We speculate that namely low-strength tethering MFN2 might participate in the fusion required to merge segments to rings as well as a specific subset of OPA1 isoforms providing such fusion at zero Δp [34]. We may expect that a cytoskeleton movement brings the two opposite ends of a short segment together.

For HEP-2G cells with FCCP the number of mitochondrial elements increased up to over 30 (Fig. 6c, d). Again new shapes were formed such as plain rings or bowl-like shapes (e.g. two separate and four integrated, Fig. 6c, d). Fig. 8a, b shows a statistically insignificant increase in tubule diameter (see also Table 1). Larger objects such as flat cisternae integrated within the remaining reticulum or separate or integrated rings (Fig. 6c, d, not counted in the variance plots) were visible also in conventional confocal 2D or 3D images (Fig. 6f, h).

3.6. Mitochondrial network morphology upon addition of both rotenone and uncoupler

Combined addition of rotenone and uncoupler simulates certain pathological states. Note that general de-energization is even more severe under these conditions, since at Δp zero also a substantial inhibition of respiration caused by rotenone is superimposed and OXPHOS is zero. We can exclude oxidative stress as a cause of the resulting changes, since rotenone-induced superoxide production is abolished by uncoupler [85]. The responses for the combination of these two agents were, however, different with INS-1E and HEP-G2 cells. For INS-1E cells the inhibition of respiration at Complex I and simultaneous uncoupling have a synergic effect (Figs. 4e, f, 5c, 9a,b; Movie V of Supplemental information). The main reticulum disintegrated into three to four parts and small morphological units increased up to 40 ($n=3$) (e.g. Fig. 5c); up to 18 small spheres and between four and 11 short segments were observed plus three to nine bowl-like objects (shell-like objects or very bulky rings) and up to three open plain rings. The bowl-like objects were a hallmark of this sample. Literally, a mixed regime of fusion/fission occurred. We speculate that even more active fusion than with FCCP alone caused super positioning of membranes onto rings, which resulted in bowl-like objects (shell-

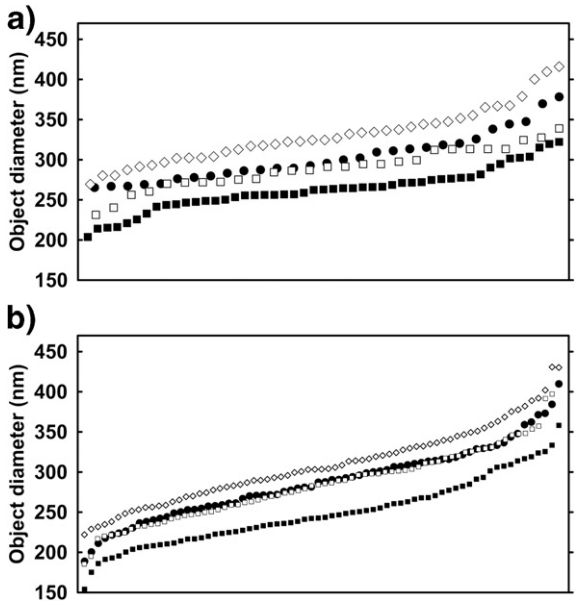

Fig. 9. Charts of tubule diameter/object size variance for disintegration of reticulum in INS-1E cells. a) PST method: The data of three to four cells (8 to 10 estimates for each) were evaluated for INS-1E cells cultivated at 11 mM glucose (black squares), and cells to which 20 μM rotenone (grey diamonds), or 1 μM FCPP (grey squares), or both, 20 μM rotenone plus 1 μM FCPP (black circles), were added for 20 min prior to fixation and imaging. Cells were imaged on the 1st instrument (see Fig. 7 legend). Diameters were derived from point-spread functions of the measured original data stacks analyzing minima and maxima of the axial intensity profile through tubules (PST method, see Ref. [74]). b) Ruler method: Symbols as in a). The data of three to four cells (70 estimates for each) are shown at points in variance distribution which represent averages within a "channel of magnitudes" of three to four cells.

like shapes or red-blood-cell-like shapes) of 0.7 to 2 μm size. Three to nine bowl-like objects were separated from the main reticulum, between two and 16 were integrated in the reticulum (n=3). The number of integrated flat cisternae decreased to 15 to 20 and number of branching points decreased to 10 to 25. In some cells also three to eight integrated rings were observed. Despite of this, fission was ongoing, at least initially, since the original nearly-single mitochondrion or single continuous reticulum disintegrated into few reticula. The diameter of remaining tubules or minimum dimensions of other objects (Fig. 9a, b) rose by ~30 nm (Table 1). In conclusion, even more pronounced fusion acting simultaneously or shortly after fission was now established and facilitated transformation of original tubules into the observed specific shapes. Analogously to uncoupling alone, we speculate that, some *pro*-fusion machinery is retained or recruited that ensures more pronounced fusion forming these specific shapes. We speculate that also strongly-tethering MFN1 might participate in this fusion.

Surprisingly, for HEP-G2 cells FCCP delayed rotenone-induced fission and *vice versa* so that it was incomplete after 30 min (Fig. 6g). Nevertheless, ring formation was still apparent even if at less abundance. Further analysis of participation of various mitodynamins and responses to de-energization and/or oxidative status is required to explain these results.

Acknowledgements

4Pi microscopic work was partly performed at Leica Microsystems facilities (Mannheim, Germany) in collaboration with Dr. Tanjef Szellas. Cell cultivation by Lenka Josková and Ing.Tomáš Špaček, and help of Martin Bartoš (Alef, Ltd., Prague) with color-coded 3D images and volume calculations are gratefully acknowledged. The project was supported by grants NR/7917-6 and NR/9183-3 from the Czech Ministry of Health; IAA500110701 and AV0Z50110509 from the Academy of Sciences, and 303/05/P100 (to L.P.-H.) from the Grant Agency of the Czech Republic. Funding for the 4Pi microscope at The Jackson Laboratory was provided by the W. M. Keck Foundation and National Science Foundation Grant DBI-0421007.

Appendix A. Supplementary data

Supplementary data associated with this article can be found, in the online version, at doi:10.1016/j.bbabio.2008.04.002.

References

[1] M.R. Duchen, Mitochondria in health and disease: perspectives on a new mitochondrial biology, Mol. Aspec. Med. 25 (2004) 365–451.
[2] L. Galluzzi, M.C. Maiuri, I. Vitale, H. Zischka, M. Castedo, L. Zitvogel, G. Kroemer, Cell death modalities: classification and pathophysiological implications, Cell Death Differ. 14 (2007) 1237–1243.
[3] S.W. Ballinger, Mitochondrial dysfunction in cardiovascular disease, Free Radic. Biol. Med. 38 (2005) 1278–1295.
[4] E. Alirol, J.C. Martinou, Mitochondria and cancer: is there a morphological connection? Oncogene 25 (2006) 4706–4716.
[5] K. Maiese, Z.Z. Chong, Y.C. Shang, Mechanistic insights into diabetes mellitus and oxidative stress, Curr. Med. Chem. 14 (2007) 1729–1738.
[6] M. Qatanani, M.A. Lazar, Mechanisms of obesity-associated insulin resistance: many choices on the menu, Genes Develop. 21 (2007) 1443–1455.
[7] M.T. Lin, M.F. Beal, Mitochondrial dysfunction and oxidative stress in neurodegenerative diseases, Nature 443 (2006) 787–795.
[8] P. Ježek, L. Hlavatá, Mitochondria in homeostasis of reactive oxygen species in cell, tissues, and organism, Int. J. Biochem. Cell Biol. 37 (2005) 2478–2503.
[9] F.L. Muller, M.S. Lustargen, Y. Jang, A. Richardson, H. Van Remmen, Trends in oxidative aging theories, Free Radic. Biol. Med. 43 (2007) 477–503.
[10] C.R. Hackenbrock, Ultrastructural bases for metabolically linked mechanical activity in mitochondria. I. Reversible ultrastructural changes with change in metabolic steady state in isolated liver mitochondria, J. Cell Biol. 30 (1966) 269–297.
[11] C.A. Mannella, Structure and dynamics of the mitochondrial inner membrane cristae, Biochim. Biophys. Acta 1763 (2006) 542–548.
[12] J. Bereiter-Hahn, M. Voth, Dynamics of mitochondria in living cells: shape changes, dislocatiions, vision and fission of mitochondria, Microsc. Res. Tech. 27 (1994) 198–219.
[13] R.J. Youle, M. Karbowski, Mitochondrial fission in apoptosis, Nat. Rev., Mol. Cell Biol. 6 (2005) 657–663.
[14] S. Hoppins, L. Lackner, J. Nunnari, The machines that divide and fuse mitochondria, Annu. Rev. Biochem. 76 (2007) 751–780.
[15] Y. Zhang, D.C. Chan, New insights into mitochondrial function, FEBS Lett. 581 (2007) 2168–2173.
[16] M. Karbowski, Y.J. Lee, B. Gaume, S.Y. Jeong, S. Frank, A. Nechushtan, A. Santel, M. Fuller, C.L. Smith, R.J. Youle, Spatial and temporal association of Bax with mitochondrial fission sites, Drp1, and Mfn2 during apoptosis, J. Cell Biol. 159 (2002) 931–938.
[17] H. Chen, A.S. Detmer, A.J. Ewald, E.E. Griffin, S.E. Fraser, D.C. Chan, Mitofusins Mfn1 and Mnf2 coordinately regulate mitochondrial fussion and are essential for embryonic development, J. Cell Biol. 160 (2003) 189–200.
[18] D. Bach, S. Pich, F.X. Soriano, N. Vega, B. Baumgartner, J. Oriola, J.R. Daugaard, J. Lloberas, M. Camps, J.R. Zierath, R. Rabasa-Lhoret, H. Wallberg-Henriksson, M. Laville, M. Palacín, H. Vidal, F. Rivera, M. Brand, A. Zorzano, Mitofusin-2 determines mitochondrial network architecture and mitochondrial metabolism. A novel regulatory mechanism altered in obesity, J. Biol. Chem. 278 (2003) 17190–17197.
[19] N. Ishihara, Y. Eura, K. Mihara, Mitofusin 1 and 2 play distinct roles in mitochondrial fusion reactions via GTPase activity, J. Cell Sci. 117 (2004) 6535–6546.
[20] H. Chen, M.F. Chomyn, D.C. Chan, Disruption of fusion results in mitochondrial heterogeneity and dysfunction, J. Biol. Chem. 280 (2005) 26185–26192.
[21] T. Koshiba, S.A. Detmer, J.T. Kaiser, H. Chen, J.M. McCaffery, D.C. Chan, Structural basis of mitochondrial tethering by mitofusin complexes, Science 305 (2004) 858–862.
[22] S.Y. Choi, P. Huang, G.M. Jenkins, D.C. Chan, J. Schiller, M.A. Frohman, A common lipid links Mfn-mediated mitochondrial fusion and SNARE-regulated exocytosis, Nat. Cell Biol. 8 (2006) 1255–1262.
[23] A.S. Detmer, D.C. Chan, Complementation between mouse Mfn1 and Mfn2 protects mitochondrial fusion defects caused by CMT2A disease mutations, J. Cell Biol. 176 (2007) 405–414.
[24] M. Karbowski, K.L. Norris, M.M. Cleland, S.-Y. Jeong, R.J. Youle, Role of Bax and Bak in mitochondrial morphogenesis, Nature 443 (2006) 658–662.
[25] S. Cipolat, O. Martins de Brito, B. Dal Zilio, L. Scorrano, OPA1 requires mitofusin 1 to promote mitochondrial fusion, Proc. Natl. Acad. Sci. U. S. A. 101 (2004) 15927–15932.
[26] C. Delettre, J.M. Griffoin, J. Kaplan, H. Dollfus, B. Lorenz, L. Faivre, G. Lenaers, P. Belenguer, C.P. Hamel, Mutation spectrum and splicing variants in the OPA1 gene, Human Genet. 109 (2001) 584–591.
[27] C. Frezza, S. Cipolat, O. Martins de Brito, M. Micaroni, G. Beznoussenko, T. Rudka, D. Bartoli, R. Polishuck, N.N. Danial, B. De Strooper, L. Scorrano, OPA1 controls apoptotic cristae remodeling independently from mitochondrial fusion, Cell 126 (2006) 177–189.
[28] S. Cipolat, T. Rudka, D. Hartmann, V. Costa, L. Serneels, K. Craessaerts, K. Metzger, C. Frezza, W. Annaert, L. D'Adamio, C. Derks, T. Dejaegere, L. Pellegrini, R. D'Hooge, L. Scorrano, B. De Strooper, Mitochondrial rhomboid PARL regulates cytochrome c release during apoptosis via OPA1-dependent cristae remodeling, Cell 126 (2006) 163–175.
[29] L. Pellegrini, L. Scorrano, A cut short to death: Parl and Opa1 in the regulation of mitochondrial morphology and apoptosis, Cell Death Differ. 14 (2007) 1275–1284.
[30] A. Olichon, E. Guillou, C. Delettre, T. Landes, L. Arnaué-Pelloquin, L.J. Emorine, V. Mils, M. Daloyau, C. Hamel, P. Amati-Bonneau, D. Bonneau, P. Reynier, G. Lenaers, P. Belanguer, Mitochondrial dynamics and disease, OPA1, Biochim. Biophys. Acta 1763 (2006) 500–509.
[31] N. Ishikara, Y. Fujita, T. Oka, K. Mihara, Regulation of mitochondrial morphology through proteolytic cleavage of OPA1, EMBO J. 25 (2006) 2966–2977.
[32] S.R. Duvezin-Caubet, J. Jagasia, S. Wagener, A. Hofmann, A. Trifunovic, A. Hansson, M.F. Chomyn, G. Bauer, N.G. Attardi, W. Larsson, W. Neupert, A.S. Reichert, Proteolytic processing of OPA1 links mitochondrial dysfunction to alterations in mitochondrial morphology, J. Biol. Chem. 281 (2006) 37972–37979.
[33] Z. Song, H. Chen, M. Fiket, C. Alexander, D.C. Chan, OPA1 processing controls mitochondrial fusion and is regulated by mRNA splicing, membrane potential, and Yme1L, J. Cell Biol. 178 (2007) 749–755.
[34] L. Griparic, T. Kanazawa, A.M. van der Bliek, Regulation of the mitochondrial dynamin-like protein Opa1 by proteolytic cleavage, J. Cell Biol. 178 (2007) 757–764.
[35] F. Malka, O. Guillery, C. Cifuentes-Diaz, E. Guillou, P. Belenguer, A. Lombès, M. Rojo, Separate fusion of outer and inner mitochondrial membranes, EMBO Rep. 6 (2005) 853–859.
[36] M. Suzuki, S-Y. Jeong, M. Karbowski, R.J. Youle, N. Tjandra, The solution structure of human mitochondria fission protein FIS1 reveals a novel TPR-like helix bundle, J. Mol. Biol. 334 (2003) 445–458.
[37] A.S. Schauss, J. Bewersdorf, S. Jakobs, Fis1p and Caf4p, but not Mdv1p are required for a polar localization of Dnm1p clusters on the mitochondrial surface, J. Cell Sci. 119 (2006) 3098–3106.
[38] M.A. Karren, E.M. Coonrod, T.K. Anderson, J.M. Shaw, The role of Fis1p–Mdv1p interactions in mitochondrial fission complex assembly, J. Cell Biol. 171 (2005) 291–301.
[39] T. Yu, R.J. Fox, L.S. Burwell, Y. Yoon, Regulation of mitochondrial fission and apoptosis by the mitochondrial outer membrane protein hFis1, J. Cell Sci. 118 (2005) 4141–4151.
[40] S. Lee, S.-Y. Jeong, W.-C. Lim, S. Kim, Y.-Y. Park, X. Sun, R.J. Youle, H. Cho, Mitochondrial fission and fusion mediators, hFis1 and OPA1, modulate cellular senescence, J. Biol. Chem. 282 (2007) 22977–22983.
[41] K.J. De Vos, V.J. Allan, A.J. Grierson, M.P. Sheetz, Mitochondrial function and actin regulate dynamin-related protein 1-dependent mitochondrial fission, Curr. Biol. 15 (2005) 678–683.

[42] S. Wasiak, R. Zunino, H.M. McBride, Bax/Bak promote sumoylation of DRP1 and its stable association with mitochondria during apoptotic cell death, J. Cell Biol. 177 (2007) 439–450.
[43] M. Karbowski, A. Neutzner, R.J. Youle, The mitochondrial E3 ubiquitin ligase MARCH5 is required for Drp1 dependent mitochondrial division, J. Cell Biol. 178 (2007) 71–84.
[44] C.-R. Chung, C. Blackstone, Cyclic AMP-dependent protein kinase phosphorylation of Drp1 regulates its GTPase activity and mitochondrial morphology, J. Biol. Chem. 282 (2007) 21583–21587.
[45] D. Tondera, A. Santel, S. Schwarzer, S. Dames, K. Giese, A. Klippel, J. Kaufmann, Knockdown of MTP18 a novel phosphatidylinositol-3-kinase-dependent protein affects mitochondrial morphology and induces apoptosis, J. Biol. Chem. 279 (2004) 31544–31555.
[46] M. Karbowski, S.-Y. Jeong, R.J. Youle, Endophilin B1 is required for the maintenance of mitochondrial morphology, J. Cell Biol. 166 (2004) 1027–1039.
[47] G.B. John, Y. Shang, L. Li, C. Renken, C.A. Mannella, J.M.L. Selker, L. Rangell, M.J. Bennett, J. Zha, The mitochondrial inner membrane protein mitofilin controls cristae morphology, Mol. Biol. Cell 16 (2005) 1543–1554.
[48] Y. Eura, N. Ishikara, T. Oka, K. Mihara, Identification of a novel protein that regulates mitochondrial fusion by modulating mitofusin (Mfn) protein function, J. Cell Sci. 119 (2006) 1913–1925.
[49] P. Hajek, A. Chomyn, G. Attardi, Identification of a novel mitochondrial complex containing mitofusin 2 and stomatin-like protein 2, J. Biol. Chem. 282 (2007) 5670–5681.
[50] G. Szabadkai, A.M. Simoni, K. Bianchi, D. De Stefani, S. Leo, M.R. Wieckowski, R. Rizzuto, Mitochondrial dynamics and Ca^{2+} signaling, Biochim. Biophys. Acta 1763 (2006) 442–449.
[51] R. Rossignol, R. Gilkerson, R. Aggeler, K. Yamagata, S.J. Remington, R.A. Capaldi, Energy substrate modulates mitochondrial structure and oxidative capacity in cancer cells, Cancer Res. 64 (2004) 985–993.
[52] G. Benard, N. Bellance, D. James, P. Parrone, H. Fernandez, T. Letellier, R. Rossignol, Mutual control of mitochondrial bioenergetics and structural network organization, J. Cell Sci. 120 (2007) 838–848.
[53] W.J.H. Koopman, S. Verkaart, H.-J. Visch, F.H. Van der Westhuizen, M.P. Murphy, L.W.P.J. Van den Heuvel, J.A.M. Smeitink, P.H.G.M. Willems, Inhibition of complex I of the electron transport chain causes O_2^--mediated mitochondrial outgrowth, Am. J. Physiol. 288 (2005) C1440–C1450.
[54] T. Yu, J.L. Robotham, Y. Yoon, Increased production of reactive oxygen species in hyperglycemic conditions requires dynamic change of mitochondrial morphology, Proc. Natl. Acad. Sci. U. S. A. 103 (2006) 2653–2658.
[55] S. Zuchner, I.V. Mersiyanova, M. Muglia, N. Bissar-Tadmouri, J. Rochelle, E.L. Dadali, M. Zappia, E. Nelis, A. Patitucci, J. Senderek, Y. Parman, O. Evgrafov, P.D. Jonghe, Y. Takahashi, S. Tsuji, M.A. Pericak-Vance, A. Quattrone, E. Battaloglu, A.V. Polyakov, V. Timmerman, J.M. Schröder, J.M. Vance, Mutations in the mitochondrial GTPase mitofusin 2 cause Charcot-Marie-Tooth neuropathy type 2 A, Nat. Genet. 36 (2004) 449–451.
[56] H.R. Waterham, et al., A lethal defect of mitochondrial and peroxisomal fission, New Engl. J. Med. 356 (2007) 1736–1741.
[57] S.A. Detmer, D.C. Chan, Functions and dysfunctions of mitochondrial dynamics, Nat. Rev., Mol. Cell Biol. 8 (2007) 870–879.
[58] M.J. Barsoun, H. Yuan, A.A. Gerentser, G. Liot, Y.E. Kushnareva, S. Graber, I. Kovacs, W.D. Lee, J. Waggoner, J. Cui, A.D. White, B. Bossy, J.-C. Martinou, R.J. Youle, S.A. Lipton, M.H. Ellisman, G.A. Perkins, E. Bossy-Wetzel, Nitric oxide-induced mitochondrial fission is regulated by dynamin-related GTPases in neurons, EMBO J. 25 (2006) 3900–3911.
[59] K.G. Lyamzaev, D.S. Izyumov, A.V. Avetisyan, F. Yang, O.Y. Pletjushkina, B.V. Chernyak, Inhibition of mitochondrial bioenergetics: the effects on structure of mitochondria in the cell and on apoptosis, Acta Biochim. Pol. 51 (2004) 553–562.
[60] O.Y. Pletjushkina, K.G. Lyamzaev, E.N. Popova, O.K. Nepryakhina, O.Y. Ivanova, L.V. Domnina, B.V. Chernyak, V.P. Skulachev, Effect of oxidative stress on dynamics of mitochondrial reticulum, Biochim. Biophys. Acta 757 (2006) 518–524.
[61] A. Aronis, J.A. Melendez, O. Golan, S. Shilo, N. Dicter, O. Tirosh, Potentiation of Fas-mediated apoptosis by attenuated production of mitochondria-derived reactive oxygen species, Cell Death Differ. 10 (2003) 335–344.
[62] G. Dispersyn, R. Nuydens, R. Connors, M. Borgers, H. Geerts, Bcl-2 protects against FCCP-induced apoptosis and mitochondrial membrane potential depolarization in PC12 cells, Biochim. Biophys. Acta 1428 (1999) 357–371.
[63] S. Kuruvilla, C.W. Qualls Jr., R.D. Tyler, S.M. Witherspoon, G.R. Benavides, L.W. Yoon, K. Dold, R.H. Brown, S. Sangiah, K.T. Morgan, Effects of minimally toxic levels of carbonyl cyanide *p*-(trifluoromethoxy) phenylhydrazone (FCCP), elucidated through differential gene expression with biochemical and morphological correlations, Toxicol. Sci. 73 (2003) 348–361.
[64] V. Desquiret, D. Loiseau, C. Jacques, O. Douay, Y. Malthiery, P. Ritz, D. Roussel, Dinitrophenol-induced mitochondrial uncoupling in vivo triggers respiratory adaptation in HepG2 cells, Biochim. Biophys. Acta 1757 (2006) 21–30.
[65] S. Meeusen, J.M. McCaffery, J. Nunnari, Mitochondrial fusion intermediates revealed in vitro, Science 305 (2004) 1747–1752.
[66] S.W. Hell, E.H.K. Stelzer, Properties of a 4Pi-confocal fluorescence microscope, J. Opt. Soc. Am. A 9 (1992) 2159–2166.
[67] S.W. Hell, E.H.K. Stelzer, Fundamental improvement of resolution with a 4Pi-confocal fluorescence microscope using two-photon excitation, Opt. Commun. 93 (1992) 277–282.
[68] K. Bahlmann, S. Jakobs, S.W. Hell, 4Pi-confocal microscopy of live cells, Ultramicroscopy 87 (2001) 155–164.
[69] H. Gugel, J. Bewersdorf, S. Jakobs, J. Engelhardt, R. Storz, S.W. Hell, Cooperative 4Pi excitation and detection yields sevenfold sharper optical sections in live-cell microscopy, Biophys. J. 87 (2004) 4146–4152.
[70] J. Bewersdorf, B.T. Bennet, K.L. Knight, H2AX chromatin structures and their response to DNA damage revealed by 4Pi microscopy, Proc. Natl. Acad. Sci. U. S. A. 103 (2006) 18137–18142.
[71] R. Medda, S. Jakobs, S.W. Hell, J. Bewersdorf, 4Pi microscopy of quantum dot-labeled cellular structures, J. Struct. Biol. 156 (2006) 517–523.
[72] S. Jakobs, High resolution imaging of live mitochondria, Biochim. Biophys. Acta 1763 (2006) 561–575.
[73] M.C. Lang, J. Engelhardt, S.W. Hell, 4Pi microscopy with linear fluorescence excitation, Opt. Lett. 32 (2007) 259–261.
[74] A. Egner, S. Jakobs, S.W. Hell, Fast 100-nm resolution three-dimensional microscope reveals structural plasticity of mitochondria in live yeast, Proc. Natl. Acad. Sci. U. S. A. 99 (2002) 3370–3375.
[75] A. Merglen, S. Theander, B. Rubi, G. Chaffard, C.B. Wollheim, P. Maechler, Glucose sensitivity and metabolism-secretion coupling studied during two-year continuous culture in INS-1E insulinoma cells, Endocrinology 145 (2004) 667–678.
[76] S.W. Hell, Far-field optical nanoscopy, Science 316 (2007) 1153–1158.
[77] B. Huang, W. Wang, M. Bates, X. Zhuang, Three-dimensional super-resolution imaging by stochastic optical reconstruction microscopy, Science 319 (2008) 810–813.
[78] E. Betzig, G.H. Patterson, R. Sougrat, O.W. Lindwasser, S. Olenych, J.S. Bonifacino, M.W. Davidson, J. Lippincott-Schwartz, H.F. Hess, Imaging intracellular fluorescent proteins at nanometer resolution, Science 313 (2006) 1642–1645.
[79] S.T. Hess, T.P.K. Girirajan, M.D. Mason, Ultra-high resolution imaging by fluorescence photoactivation localization microscopy, Biophys. J. 91 (2006) 4258–4272.
[80] A. Egner, C. Geisler, C. von Middendorff, H. Bock, D. Wenzel, R. Medda, M. Andresen, A.C. Stiel, S. Jakobs, C. Eggeling, A. Schönle, S.W. Hell, Fluorescence nanoscopy in whole cells by asynchronous localization of photoswitching emitters, Biophys. J. 93 (2007) 3285–3290.
[81] K.I. Willig, B. Harke, R. Medda, S.W. Hell, STED microscopy with continuous wave beams, Nat. Methods 4 (2007) 915–918.
[82] M.F. Juette, T.J. Gould, M.D. Lessard, M.J. Mlodzianoski, B.S. Nagpure, B.T. Bennett, S.T. Hess, J. Bewersdorf, Three-dimensional sub-100 nm resolution fluorescence microscopy of thick samples, Nat. Methods (in press) (11 May 2008, Electronic publication ahead of print), doi:10.1038/nmeth.1211.
[83] A. Egner, S. Verrier, A. Goroshkov, H.D. Söling, S.W. Hell, 4Pi-microscopy of the Golgi apparatus in live mammalian cells, J. Struct. Biol. 147 (2004) 70–76.
[84] T. Špaček, Z. Berková, K. Zacharovová, L. Hlavatá, J. Šantorová, F. Saudek, P. Ježek, Glucose stimulated-insulin secretion of insulinoma INS1-E cells is associated with elevation of both respiration and mitochondrial membrane potential, Int. J. Biochem. & Cell Biol. 40 (2008) 1522–1535.
[85] A. Dlasková, L. Hlavatá, P. Ježek, Oxidative stress caused by blocking of mitochondrial Complex I H^+ pumping as a link in aging/disease vicious cycle. Int. J. Biochem. & Cell Biol. http://dx.doi.org/10.1016/j.biocel.2008.01.012.